

Article

Sol-Gel Glass-Ceramic Materials Containing $\text{CaF}_2:\text{Eu}^{3+}$ Fluoride Nanocrystals for Reddish-Orange Photoluminescence Applications

Natalia Pawlik ^{1,*}, Barbara Szpikowska-Sroka ¹, Tomasz Goryczka ² and Wojciech A. Pisarski ^{1,*}¹ Institute of Chemistry, University of Silesia, 40-007 Katowice, Poland; barbara.szpikowska-sroka@us.edu.pl² Institute of Materials Engineering, University of Silesia, 41-500 Chorzów, Poland; tomasz.goryczka@us.edu.pl

* Correspondence: natalia.pawlik@smcebi.edu.pl (N.P.); wojciech.pisarski@us.edu.pl (W.A.P.)

Received: 14 November 2019; Accepted: 9 December 2019; Published: 13 December 2019



Abstract: $\text{CaF}_2:\text{Eu}^{3+}$ glass-ceramic sol-gel materials have been examined for reddish-orange photoluminescence applications. The transformation from precursor xerogels to glass-ceramic materials with dispersed fluoride nanocrystals was verified using several experimental methods: differential scanning calorimetry (DSC), thermogravimetric analysis (TG), X-ray diffraction (XRD), transmission electron microscopy (TEM), infrared spectroscopy (IR-ATR), energy dispersive X-ray spectroscopy (EDS) and photoluminescence measurements. Based on luminescence spectra and their decays, the optical behavior of Eu^{3+} ions in fabricated glass-ceramics were characterized and compared to those of precursor xerogels. In particular, the determined luminescence lifetime of the $^5\text{D}_0$ excited state of Eu^{3+} ions in nanocrystalline $\text{CaF}_2:\text{Eu}^{3+}$ glass-ceramic materials is significantly prolonged in comparison with prepared xerogels. The integrated intensities of emission bands associated to the $^5\text{D}_0 \rightarrow ^7\text{F}_2$ electric-dipole transition (ED) and the $^5\text{D}_0 \rightarrow ^7\text{F}_1$ magnetic-dipole transition (MD) are changed drastically during controlled ceramization process of xerogels. This implies the efficient migration of Eu^{3+} ions from amorphous silicate sol-gel network into low-phonon energy CaF_2 nanocrystals.

Keywords: CaF_2 nanocrystals; glass-ceramics; Eu^{3+} luminescence; sol-gel synthesis

1. Introduction

Transparent glass-ceramics (GCs) containing fluoride nanocrystals fabricated using high-temperature melt-quenching or low-temperature sol-gel method are suitable modern materials for lasers, optical waveguides, solid-state lighting and numerous photonic applications [1–5]. Depending on chemical composition and technological conditions, nano- or micro-crystals are usually well-formed during temperature-controlled crystallization of precursor glasses or xerogels. The heat-treatment process often introduces transformation from amorphous systems to transparent oxyfluoride glass-ceramic materials and rare earths play the role as optically active ions. The coordination sphere around rare earth ions changes drastically during this structural transformation, giving important contribution to the luminescence characteristics.

Among binary and ternary rare-earth fluoride nanophosphors [6], calcium fluoride CaF_2 belongs to the most important and perspective nanoparticles, which could be successfully formed during the heat treatment process. CaF_2 fluoride nanocrystals were well formed from $\text{Na}_2\text{O}/\text{K}_2\text{O}/\text{CaO}/\text{CaF}_2/\text{Al}_2\text{O}_3/\text{SiO}_2$ glass [7] and their mean crystallite sizes were in the range from 8 to 10.4 nm and did not get larger with time or increasing the annealing temperature. However, synthesis, structure and properties of transparent glass-ceramics containing CaF_2 nanocrystals depended critically on treating temperature

and glass composition, where SiO₂ was substituted by CaO/CaF₂ [8]. A special attention has been paid to crystallization processes and spectroscopic properties of erbium-doped transparent glass ceramics containing CaF₂ nanocrystals [9–11]. In this CaF₂:Er³⁺ glass-ceramic system, near-IR luminescence at 1.53 μm [12,13] and up-conversion processes [14,15] of Er³⁺ ions have been examined in detail. The results for the crystallization processes and fluorescence properties of Nd³⁺-doped glass-ceramics with CaF₂ nanocrystals have been also presented and discussed [16,17]. Recently, several research groups have been focused on glass-ceramic materials containing CaF₂ nanocrystals for numerous photonic applications. Seo et al. [18] suggest that CaF₂:Dy³⁺ nano-glass-ceramics are promising for white light generation. Moreover, the oxyfluoride glass-ceramics containing CaF₂:Sm³⁺ crystals have become a new fast erasable dosimetric detector material for micro-beam radiation cancer therapy applications at the Canadian Synchrotron [19].

In this work, oxyfluoride silicate xerogels containing europium ions were heat-treated at 350 °C to obtain transparent glass-ceramics containing crystalline fluoride nano-phase CaF₂. Luminescence spectra of Eu³⁺ ions and their decays in transparent glass-ceramic samples have been studied and compared to precursor silicate xerogels. Our previously published work indicates that sol-gel glass-ceramics containing SrF₂:Eu³⁺ fluoride nanocrystals are attractive materials for reddish-orange luminescence applications [20].

2. Materials and Methods

The reagents used during proposed sol-gel synthesis were from the Aldrich Chemical Company and contained analytical purity. Deionized water was taken from an Elix 3 system (Millipore, Molsheim, France).

The Eu³⁺-doped xerogels with nominal composition (in molar ratio): TEOS:C₂H₅OH:H₂O:CH₃COOH = 1:4:10:0.5 (90 wt.%) CF₃COOH:Ca(CH₃COO)₂:Eu(CH₃COO)₃ = 5:1:0.05 (10 wt.%) were synthesized. In the presented procedure, the mixtures of tetraethoxysilane (TEOS), ethanol, water and acetic acid were put into round-bottom flasks and stirred for 30 min to perform the hydrolysis reaction. Simultaneously, Ca(CH₃COO)₂ and Eu(CH₃COO)₃ were dissolved in water and trifluoroacetic acid (TFA). In the next step, the obtained solutions were introduced into hydrolyzed tetraethoxysilane (TEOS) and mixed for another 60 min. After this time, the sols were dried at 35 °C for seven weeks to form transparent and colorless xerogels. To fabricate the glass-ceramics containing CaF₂ nanocrystals, the xerogels were heat-treated in a muffle furnace FCF 5 5SHP (Czylok, Jastrzębie-Zdrój, Poland) at 350 °C. The temperature was raised by 10 °C/min until the direct temperature (350 °C) was achieved and the xerogels were heat-treated for 10 h. Afterwards, resulted glass-ceramic materials were cooled down to room temperature in a closed furnace.

Fabricated samples were characterized by a SETARAM Labsys thermal analyzer (SETARAM Instrumentation, Caluire, France) using the thermogravimetric analysis (TG) and differential scanning calorimetry (DSC) method. The DSC curves were acquired with heating rate of 10 °C/min and the curves were registered within temperature range from 40 °C to 500 °C. To verify the crystallization of the CaF₂ phase, the X-ray diffraction (XRD) analysis was carried out using an X'Pert Pro diffractometer supplied by PANalytical (Almelo, The Netherlands) with Cu Kα radiation. The TEM microscopy was also used and the CaF₂ nanocrystals were observed via a JEOL JEM 3010 electron transmission microscope (JEOL, Tokyo, Japan) operated at 300 kV. To determine the distribution of chemical elements in studied CaF₂:Eu³⁺ GCs, an energy dispersive X-ray spectroscopy (EDS) analysis was also performed using JEOL microscope. To examine the structural changes within silicate network during controlled heat-treatment, the infrared spectroscopy (IR-ATR) spectra were registered using the Nicolet iS50 ATR spectrometer (Thermo Fisher Scientific, Waltham, MA, USA) in the frequency region 500 cm⁻¹–4000 cm⁻¹. The luminescence measurements were carried out using a Horiba Jobin-Yvon FluoroMax-4 spectrofluorimeter (Horiba Jobin Yvon, Longjumeau, France) equipped with 150 W xenon lamp. The spectral resolution was ±0.1 nm. Decay curves were detected with the accuracy of ±2 μs. All structural and photoluminescence measurements were performed at room temperature.

3. Results and Discussion

3.1. Structural and Thermal Characterization of Sol-Gel Materials

Firstly, the IR-ATR technique was used for identification the chemical bonding and functional groups inside prepared sol-gel materials and the results are presented in Figure 1. To verify the structural changes during transformation of xerogels into $\text{CaF}_2:\text{Eu}^{3+}$ GCs, the infrared spectra were recorded in the 500 cm^{-1} – 4000 cm^{-1} frequency region. The assignment of recorded infrared signals was carried out based on current literature [21,22]. For xerogels obtained after seven weeks from synthesis, the creation of three-dimensional silicate network was confirmed. Indeed, the presence of infrared (IR) signals near 1193 cm^{-1} , 799 cm^{-1} (Si-O-Si siloxane bridges), 1134 cm^{-1} , 1044 cm^{-1} and 963 cm^{-1} (Q^n units in SiO_4 tetrahedrons: Q^4 , Q^3 and Q^2 , respectively) indicates that polycondensation reaction occurred. In addition, we identified the presence of vicinal or geminal Si-OH groups ($\sim 3664\text{ cm}^{-1}$), hydrogen-bonded Si-OH moieties ($\sim 3398\text{ cm}^{-1}$) and hydrogen-bonded OH groups ($\sim 3233\text{ cm}^{-1}$) originated from residual organic solvents and water. The IR signals located at 1664 cm^{-1} (C = O groups vibrations) as well as 1447 cm^{-1} (C-H vibrations) also confirmed that the porous sol-gel network was filled by liquids. It should be noted that the infrared peak at $\sim 1664\text{ cm}^{-1}$ frequency region was also assigned to adsorbed water and Si-OH groups. Moreover, the presence of un-decomposed calcium and europium (III) trifluoroacetates was also confirmed (1193 cm^{-1} , 1134 cm^{-1}).

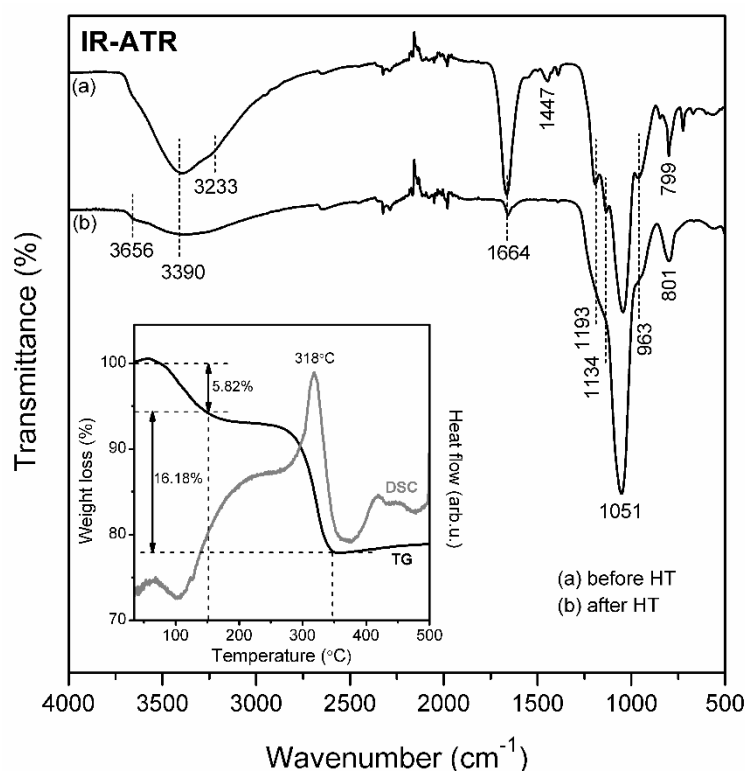
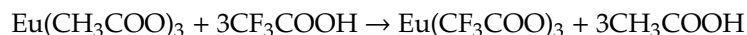
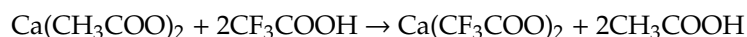


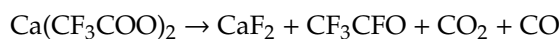
Figure 1. Infrared spectroscopy (IR-ATR) spectra of sol-gel materials before and after controlled heat-treatment. Inset shows the thermogravimetric analysis (TG)/differential scanning calorimetry (DSC) curves recorded for prepared xerogels.

To evaluate the thermal resistance of precursor xerogels and to identify the crystallization temperature, the TG/DSC analysis was performed in a temperature range from $35\text{ }^{\circ}\text{C}$ up to $500\text{ }^{\circ}\text{C}$ (inset of Figure 1). The thermal degradation profile with two distinguishable stages was recorded in temperature intervals: $35\text{ }^{\circ}\text{C}$ – $151\text{ }^{\circ}\text{C}$ (1) and $151\text{ }^{\circ}\text{C}$ – $348\text{ }^{\circ}\text{C}$ (2). For prepared xerogels, the first stage was recorded as a gentle degradation. An indicated step could be associated with desorption of ethanol and water as well as acetic acid and the accompanying weight-loss was estimated to be 5.82%.

Beyond the residual acetic acid (used as a catalyst), such acid was also produced during the chemical reaction between TFA and acetate salts:



As was shown, CF_3COO^- anions could effectively coordinate RE^{3+} cations, therefore, the trifluoroacetate ions were chemically bonded. In fact, TFA was introduced as fluorination agent, which allowed for successful precipitation of CaF_2 crystal fraction during the heat-treatment of xerogels. Finally, the next TG step for prepared sol-gel samples could be associated with the thermal decomposition of $\text{Ca}(\text{CF}_3\text{COO})_2$ and the formation of CaF_2 nanocrystals. The formation of the CaF_2 fluoride phase was realized by a homogeneous nucleation through a controlled fluorination, when the Ca-O bond cleaved and the Ca-F bond was formed [23]. The CaF_2 crystal phase was obtained during thermal decomposition of $\text{Ca}(\text{CF}_3\text{COO})_2$ as follows:



The decomposition of $\text{Ca}(\text{CF}_3\text{COO})_2$ was observed in DSC curve as an exothermic peak with maximum at ~ 318 °C. Generally, such a second degradation step was observed in recorded TG curves as a relatively high weight-loss, which was estimated to 16.18%. Based on presented TG/DSC results, the $T = 350$ °C was chosen to perform the controlled ceramization process of precursor xerogels in order to precipitate the CaF_2 nanocrystals dispersed in silicate sol-gel host. Furthermore, the resultant sol-gel materials were almost completely thermally stable at the indicated temperature level.

As was proven by infrared measurements performed after controlled heat-treatment process, the significant changes in shape of recorded spectra were well-visible. The recorded infrared signals were identified as vibrations that originated from the silicate framework. It was observed that the broad OH-band significantly decreased in intensity, and indicated the evaporation of volatile components (disappearance of maximum located at 3233 cm^{-1}) as well as progressive polycondensation reaction of silicate network (reduction in intensity of maximum at 3390 cm^{-1}). The weak peak at $\sim 1664 \text{ cm}^{-1}$ was also detected and it was associated to residual Si-OH groups. For heat-treated samples, the shoulders located at $\sim 1193 \text{ cm}^{-1}$ and $\sim 1134 \text{ cm}^{-1}$ were related to Si-O-Si siloxane bridges and SiO_4 tetrahedrons in Q^4 units, respectively. Otherwise, the vibration modes originated from SiO_4 tetrahedrons inside Q^3 (1051 cm^{-1}) and Q^2 units (951 cm^{-1}) were also identified. Indeed, it growth in density from 1.936 g/cm^3 before controlled ceramization up to 2.201 g/cm^3 for the heat-treated sample.

The influence of controlled heat-treatment process was also evaluated using XRD measurements and the results are depicted in Figure 2a. For xerogels, a broad halo pattern was recorded and it indicated their amorphous nature without long-range order. The diffraction lines were observed after performed controlled ceramization process at 350 °C per 10 h. The XRD patterns are in good accordance with the diffraction lines of regular CaF_2 phase from ICDD (The International Centre for Diffraction Data, PDF-2 No. 65-0535) crystallized in the $\text{Fm}3\text{m}$ space group. The subsequent diffraction lines at 28.2° , 46.9° , 55.6° , 68.6° and 75.8° were identified as (111), (200), (311), (400) and (311) reflexes of CaF_2 phase, respectively. Observed broadening of diffraction lines clearly indicates that CaF_2 phase crystallized in nanometric range and the average crystals size was estimated using the Scherrer formula:

$$D = \frac{K\lambda}{\beta \cos \theta} \quad (1)$$

in which D is related to the crystal size, K is a constant value (for our calculations it was taken $K = 1$), λ is the X-ray wavelength, β is a half width of analyzed diffraction peak and θ is the diffraction angle. The mean value of CaF_2 nanocrystals was equaled to $11.7 \text{ nm} \pm 1.0 \text{ nm}$. Due to similar ionic radii of Ca^{2+} (1.00 \AA) [24] and Eu^{3+} (1.07 \AA) [25], Ca^{2+} cations in CaF_2 crystal lattice could be effectively substituted by trivalent Eu^{3+} ions and therefore, a very slight shift of diffraction lines was identified.

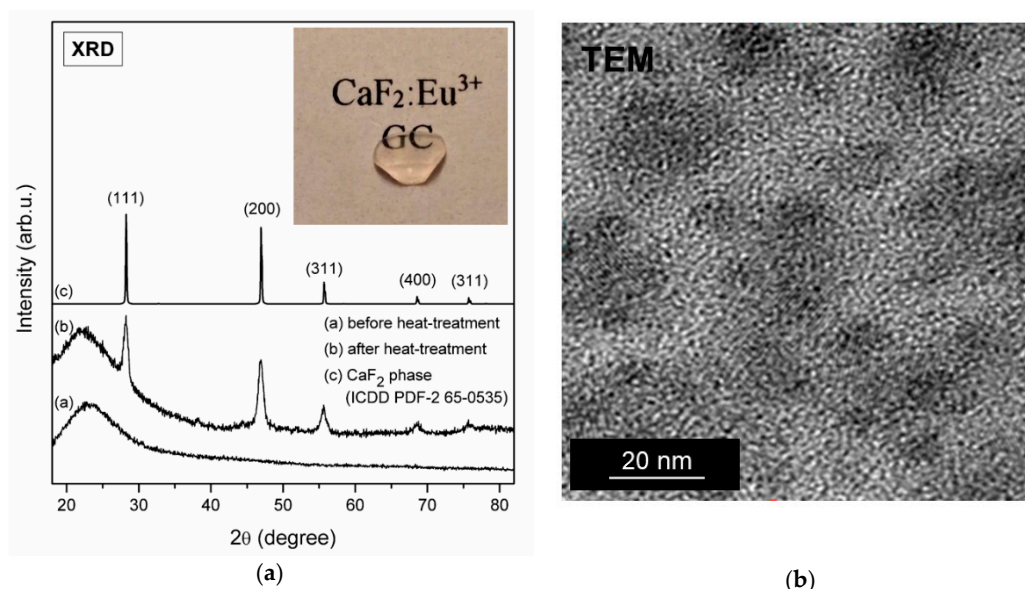


Figure 2. (a) X-ray diffraction (XRD) patterns for xerogel and $\text{CaF}_2:\text{Eu}^{3+}$ glass-ceramic fabricated during controlled heat-treatment at 350 °C. Inset shows the image of glass-ceramic (GC) sample; (b) transmission electron microscopy (TEM) image of $\text{CaF}_2:\text{Eu}^{3+}$ nanocrystals dispersed within amorphous sol-gel host.

Figure 2b presents TEM image of fabricated glass-ceramics. The size of CaF_2 nanocrystals was consistent with average crystal size estimated from Scherrer equation. The CaF_2 nanocrystals with comparable size (about 10 nm) were obtained by Zhou et al. [26] in GCs fabricated during ceramization of precursor glasses with composition $(45\text{SiO}_2-25\text{CaF}_2-20\text{Al}_2\text{O}_3-10\text{CaO}):4\%\text{EuF}_3$ (treatment conditions: 700 °C/4 h). In addition, to verify the quantitative distribution of chemical elements in fabricated glass-ceramics, we carried out the analysis from the selected sample area containing CaF_2 nanocrystal using energy dispersive X-ray spectroscopy, EDS. Generally, the content of Ca and F in CaF_2 nanocrystal were estimated to 5 wt.% and 6 wt.%, respectively; and the content of Si and O from silicate sol-gel matrix were estimated to 41 wt.% and 48 wt.%, respectively. Since Eu^{3+} ions were introduced during sol-gel synthesis as a dopant, their concentration was below the quantification limit and determination their quantitative distribution between CaF_2 nanocrystals and a silicate host was not possible. Moreover, according to another data presented in literature, we proposed the lowest treatment temperature (350 °C) to the fabrication of $\text{CaF}_2:\text{Eu}^{3+}$ glass-ceramic materials (550 °C–570 °C [27], 620 °C–680 °C [28], 660 °C [29], 800 °C [30]). Nowadays, the low-temperature processes are preferable and therefore, the formation of CaF_2 nanocrystals at 350 °C seems to be highly desirable.

Based on weight-loss during sol-gel transformation from initial liquid sol to xerogel and taking the results from TG/DSC analysis into account, we estimated the amount of CaF_2 crystal fraction in the prepared GC sample. In general, it was found that during successive evaporation of volatile components (water and organic compounds used during synthesis) and progressive polycondensation reaction of silicate network, the remaining mass of fabricated xerogel was evaluated on 16.7 wt.% of the initial sol weight. Based on the TG curve shown in Figure 1, the total weight loss during heat-treatment could be estimated to about 22.0 wt.%. The second degradation step was strictly associated with thermal decomposition of $\text{Ca}(\text{CF}_3\text{COO})_2$ and the indicated weight-loss (16.18 wt.%) should be related with evaporation of CF_3CFO , CO_2 as well as CO . Therefore, based on above results and taking the stoichiometry of thermal degradation reaction of $\text{Ca}(\text{CF}_3\text{COO})_2$ into account, the amount of CaF_2 crystal fraction was estimated to about 8 wt.% (simultaneously, the estimated mass of silicate sol-gel host is about 92 wt.%). Moreover, based on performed calculations, it was assumed that thermal degradation should be complete (it should be also noted that the amount of introduced $\text{Ca}(\text{CH}_3\text{COO})_2$ salt into reaction system during sol-gel synthesis was only 2.3 wt.%).

3.2. Luminescence Behavior of Fabricated Sol-Gel Materials

Figure 3 shows the photoluminescence excitation spectra (PLE) of prepared xerogels and $\text{CaF}_2:\text{Eu}^{3+}$ glass-ceramics. The spectra were monitored at $\lambda_{\text{em}} = 611 \text{ nm}$ wavelength corresponding to the ${}^5\text{D}_0 \rightarrow {}^7\text{F}_2$ optical transition of Eu^{3+} ions. The recorded excitation lines were identified as the intra-configurational electronic transitions inside $4f^6$ manifold of Eu^{3+} optically active ions. The bands were assigned to transitions from the ${}^7\text{F}_0$ ground level to the excited states: ${}^5\text{D}_4$ (363 nm), ${}^5\text{G}_1$, ${}^5\text{L}_7$ (372 nm–389 nm), ${}^5\text{L}_6$ (395 nm–xerogel, 394 nm/398 nm– $\text{CaF}_2:\text{Eu}^{3+}$ GCs) and ${}^5\text{D}_2$ (465 nm–xerogel, 464 nm– $\text{CaF}_2:\text{Eu}^{3+}$ GCs). In addition, the weak bands according to the ${}^7\text{F}_0 \rightarrow {}^5\text{D}_3$ (416 nm) and ${}^7\text{F}_0 \rightarrow {}^5\text{D}_1$ (525 nm) transitions were recorded. Since, the ${}^7\text{F}_1$ level is thermally populated at room temperature, a satellite line corresponding to the ${}^7\text{F}_1 \rightarrow {}^5\text{D}_1$ (535 nm) was also observed.

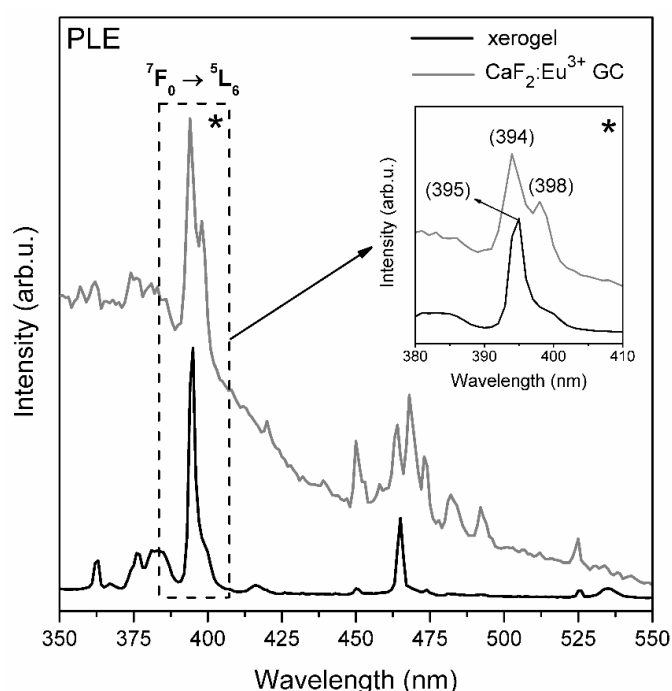


Figure 3. Photoluminescence excitation spectra (PLE) spectra registered for fabricated xerogels and $\text{CaF}_2:\text{Eu}^{3+}$ GCs.

It was observed that for xerogels the ${}^7\text{F}_0 \rightarrow {}^5\text{L}_6$ excitation band has only one maximum, meanwhile for prepared $\text{CaF}_2:\text{Eu}^{3+}$ GC samples such a line is a double peak with two splitted components located at 394 nm and 398 nm. Since Eu^{3+} ions could be distributed between silicate sol-gel host and CaF_2 nanocrystals in fabricated GCs, such splitting into two components could indicate that Eu^{3+} ions are residing in two different frameworks, as was suggested by A.C. Yanes for sol-gel $\text{LaF}_3:\text{Eu}^{3+}$ GCs [31]. Thus, 394 nm component could be associated with their location within silicate network, meanwhile 398 nm component could be related with location of Eu^{3+} in fluoride nanocrystals. Based on paper by J. Pan et al. [32], the excitation spectra of pure $\text{CaF}_2:\text{Eu}^{3+}$ crystal phase revealed only one component of the ${}^7\text{F}_0 \rightarrow {}^5\text{L}_6$ band. Therefore, it may confirm the hypothesis that visible splitting of indicated excitation band could be related with distribution of Eu^{3+} ions between CaF_2 nanocrystals and silicate sol-gel host. Since the most intense excitation line corresponded to the ${}^7\text{F}_0 \rightarrow {}^5\text{L}_6$ transition for fabricated sol-gel samples, the appropriate wavelengths were used to perform the emission measurements.

The photoluminescence spectrum (PL) registered for precursor xerogels is shown in Figure 4. Generally, the recorded spectrum consisted from five emission bands assigned to the transitions from the ${}^5\text{D}_0$ excited state into the ${}^7\text{F}_j$ levels: ${}^7\text{F}_0$ (578 nm), ${}^7\text{F}_1$ (591 nm), ${}^7\text{F}_2$ (616 nm), ${}^7\text{F}_3$ (649 nm) as well as ${}^7\text{F}_4$ (697 nm). Since the relative intensities of Eu^{3+} emission bands were strictly dependent on symmetry in their local framework, the emission spectra gave valuable information about the nearest

framework around them in host matrix [32]. It was observed that for silicate xerogels an emission band assigned to the $^5D_0 \rightarrow ^7F_2$ electric-dipole transition was more intense compared to a line assigned to the $^5D_0 \rightarrow ^7F_1$ magnetic-dipole transition. The $^5D_0 \rightarrow ^7F_2$ transition was very sensitive to the symmetry in the local vicinity around Eu^{3+} ions and it was hypersensitive in nature. Conversely, an intensity of the $^5D_0 \rightarrow ^7F_1$ band was rather independent on the symmetry in nearest surrounding of Eu^{3+} ions. Hence, the ratio between the $^5D_0 \rightarrow ^7F_2$ and the $^5D_0 \rightarrow ^7F_1$ emission intensities—well-known as R/O—can play the role as a useful tool for estimating the symmetry in which Eu^{3+} ions are located [33,34]. The R/O-ratio value calculated for prepared xerogels was estimated to be 4.13.

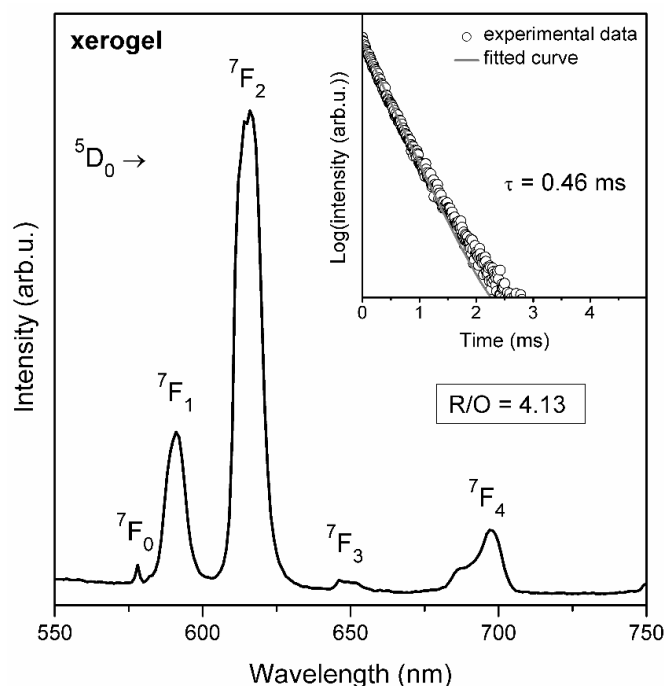


Figure 4. Photoluminescence spectrum (PL) spectra recorded for silicate xerogels. Inset presents the luminescence decay curve of the 5D_0 state of Eu^{3+} ($\lambda_{\text{exc}} = 395 \text{ nm}$, $\lambda_{\text{em}} = 591 \text{ nm}$).

Furthermore, as was shown in the inset of Figure 4, the luminescence decay curve registered for precursor xerogels was well-fitted to the mono-exponential function and the estimated luminescence lifetime of the 5D_0 state was estimated to be $\tau = 0.46 \text{ ms}$. The short luminescence lifetime was strictly related with the structure of fabricated xerogels. The luminescence from the 5D_0 state was quenched by numerous OH groups in local framework of Eu^{3+} ions and such groups originated from silanol Si-OH moieties (3664 cm^{-1} , 3398 cm^{-1}) as well as residual water and organic solvents (3233 cm^{-1}) inside the porous silicate network. Since the $^5D_0 \rightarrow ^7F_6$ energy gap of Eu^{3+} ions was equal to $\Delta E = 12,500 \text{ cm}^{-1}$ [35], only about four OH phonons were required to promote a non-radiative deactivation of the 5D_0 excited level. Since CF_3COO^- anions were in the coordination sphere around Eu^{3+} cations, it should be noted that such non-radiative relaxation from the 5D_0 state could be also caused by C = O groups (1664 cm^{-1} , eight phonons) and the C-F bond (1193 cm^{-1} , ten phonons). However, among identified functional groups, we expected that OH moieties could play a major role in non-radiative deactivation. In general, the non-radiative rates of intra-configurational $4f^n-4f^n$ transitions of rare earths were exponentially dependent on the energy gap (ΔE) and the phonon energy in their nearest surrounding ($\hbar\omega$). Such correlation is well-known as the energy gap law and it states that an increase in the non-radiative decay rate is assisted by a decreasing number of phonons needed to cover the energy gap, ΔE . Hence, if there is a functional group with high vibrational energy in a local framework of Eu^{3+} ions, the probability of non-radiative multiphonon relaxation increases. The phonons with maximum energy in a host are also usually called as effective phonons

($\hbar\omega_{\max}$) [36,37]. The influence of different types of functional groups in Eu^{3+} -doped silicate glasses on multiphonon relaxation was discussed in work by A. Herrmann et al. [38]. The rates of multiphonon relaxation, k_{NR} , via OH modes (3750 cm^{-1} , $k_{\text{NR}} = 1.4 \times 10^{-2} \text{ s}^{-1}$) and Si-O vibrations (1250 cm^{-1} , $k_{\text{NR}} = 9.0 \times 10^{-13} \text{ s}^{-1}$) clearly indicates that OH groups with maximum phonon energy in studied glasses play a major role in quenching the luminescence from the $^5\text{D}_0$ state. Moreover, the luminescence lifetime is not dependent only on phonon energy in the nearest framework around the optically active ion, but also on another factors, like symmetry. In general, the lower the symmetry is in the nearest vicinity of Eu^{3+} ion, the more allowed are the forbidden f-f transitions. Therefore, taking the symmetry aspect into account, the probability of radiative relaxation is relatively high, which results in a short luminescence lifetime.

As was presented in Figure 5, the emission spectrum of $\text{CaF}_2:\text{Eu}^{3+}$ GCs also consisted of the characteristic bands of Eu^{3+} ions corresponding to the intra-configurational $^5\text{D}_0 \rightarrow ^7\text{F}_J$ transitions within the $4f^6$ manifold. Such bands were recorded at the following wavelengths: 577 nm ($J = 0$), 589 nm ($J = 1$), 613 nm ($J = 2$), 648 nm ($J = 3$), 683 nm/689 nm/699 nm ($J = 4$). Compared to xerogels, a significant growth in intensity of the orange $^5\text{D}_0 \rightarrow ^7\text{F}_1$ band was observed and it was accompanied by eight-fold decrease in the R/O-ratio value (from 4.13 to 0.51). The indicated decline in the R/O-ratio value clearly points to the change in the symmetry in the nearest vicinity around dopant ions and the nature of the bonding character between Eu^{3+} ions and their nearest surrounding covalent to become more ionic. Obviously, this is related with the partial incorporation of optically active ions into the crystallized CaF_2 fluoride phase.

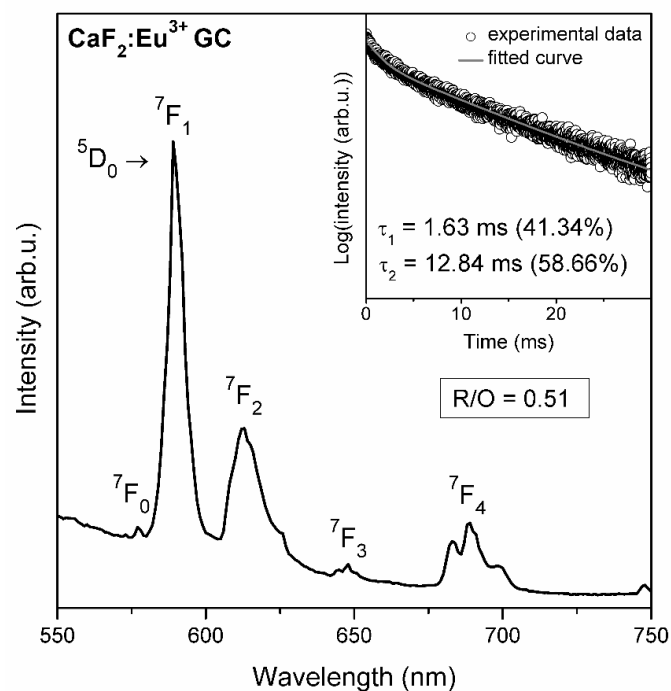


Figure 5. PL spectra recorded for fabricated $\text{CaF}_2:\text{Eu}^{3+}$ GCs. The inset presents the luminescence decay curve of the $^5\text{D}_0$ state of Eu^{3+} ($\lambda_{\text{exc}} = 394 \text{ nm}$, $\lambda_{\text{em}} = 589 \text{ nm}$).

The $^7\text{F}_J$ energy levels of Eu^{3+} ions in crystal lattice could split and the number of individual sublevels depends on the J number and the site symmetry [33]. According to paper by Brown et al. [39], Eu^{3+} ions are located in C_{4v} symmetry sites in the CaF_2 crystal lattice, despite the fact that Ca^{2+} cations are located in O_h symmetry sites. This effect could be explained by charge compensation, when divalent Ca^{2+} cations in CaF_2 crystal lattice are substituted by trivalent Eu^{3+} ions. Then, due to prevent the non-equilibrium charge in the crystal lattice, cation vacancies could be also formed and some fluorine anions could occupy the interstitial positions. If the Eu^{3+} ion is located in the C_{4v} site in the CaF_2 crystal

lattice, the individual ${}^5D_0 \rightarrow {}^7F_J$ ($J = 0-4$) band should split into one ($J = 0$), two ($J = 1$), four ($J = 2$), five ($J = 3$) and seven ($J = 4$) components. However, the distinguishing of individual components was quite difficult for fabricated glass-ceramic samples, because Eu^{3+} ions are distributed both in amorphous silicate sol-gel network as well as CaF_2 nanocrystals. Hence, we assumed that the influence of the crystal field is largely masked.

The photoluminescence decay curve of the 5D_0 state of Eu^{3+} ions recorded for fabricated glass-ceramics was presented in the inset of Figure 5. The decay curve was well-fitted to double-exponential function and therefore, it was distinguished two different decay components: fast ($\tau_1 = 1.63$ ms) and slow ($\tau_2 = 12.84$ ms). The double-exponential decay clearly indicates that two different decay channels are involved in the total decay process from the 5D_0 excited state of Eu^{3+} . The contribution of fast and slow components could be determined using fitting constants in the following equation:

$$\tau_n, \% = \frac{A_n}{A_n + A_m} \cdot 100\% \quad (2)$$

Since the A_1 and A_2 fitting constants were close to 1.9408×10^6 and 2.7539×10^6 , respectively, a percentage contribution of τ_1 was equal to 41.34% and the contribution of τ_2 was 58.66%. The first of the luminescence lifetime, τ_1 , was associated with Eu^{3+} ions located in the silicate sol-gel host consisting of Q^3 units of SiO_4 tetrahedrons ($\sim 1051 \text{ cm}^{-1}$) and residual Si-OH groups (3390 cm^{-1} , 3656 cm^{-1}). In this way, to cover the energy gap in silicate host, four Si-OH groups or twelve Q^3 units were needed. The second luminescence lifetime component, τ_2 , was related with the remaining part of Eu^{3+} ions which were successfully incorporated into CaF_2 nanocrystals during the controlled heat-treatment process. Indeed, due to low-phonon energy of the CaF_2 crystal lattice ($\sim 466 \text{ cm}^{-1}$ [40]), about 27 Ca-F phonons were needed to cover the ${}^5D_0 \rightarrow {}^7F_6$ energy gap. The probability of non-radiative relaxation from the 5D_0 state was greater within the silicate framework than in the CaF_2 crystal lattice due to higher-phonon energies. Moreover, the probability of radiative relaxation was lower in more symmetric CaF_2 than in asymmetric sol-gel host. Therefore, the τ_2 components were significantly prolonged compared to τ_1 . Moreover, we suggested that the tendency of the Eu^{3+} ions to migrate into CaF_2 could be promoted by a similar ionic radii of Ca^{2+} (1.00 \AA) and Eu^{3+} (1.07 \AA). It should be also noted that the τ_1 luminescence lifetime component of fabricated $\text{CaF}_2:\text{Eu}^{3+}$ GCs was prolonged compared with the τ lifetime estimated for xerogel. Both of the presented lifetimes were related with Eu^{3+} ions, which were dispersed inside the silicate sol-gel host. To explain the differences in luminescence lifetime values, we used the results from the IR-ATR spectroscopy. As was evidenced by IR measurements, the huge amounts of OH groups with high vibrational energies (above 3000 cm^{-1}) were identified in the structure of fabricated xerogels. Therefore, such numerous OH groups in the nearest vicinity of Eu^{3+} ions were mainly responsible for non-radiative quenching of luminescence from the 5D_0 excited state, which resulted in a relatively short lifetime. Simultaneously, the infrared measurements carried out for $\text{CaF}_2:\text{Eu}^{3+}$ glass-ceramic indicated a strong reduction of OH groups, hence, the amount of effective 'quenchers' in the nearest surrounding of Eu^{3+} ions in the silicate sol-gel network was smaller than in xerogels. In consequence, the τ_1 luminescence lifetime was prolonged due to smaller amounts of OH quenchers.

4. Conclusions

Transparent glass-ceramic materials containing CaF_2 fluoride nanocrystals were prepared by a low-temperature sol-gel route. Thermal decomposition of $\text{Ca}(\text{CF}_3\text{COO})_2$ in xerogels was confirmed by using TG/DSC methods. The formation of CaF_2 nanocrystals during the heat-treatment process was confirmed by X-ray diffraction measurements and TEM microscopy. The structural changes in the sol-gel silica-network were verified by the IR-ATR spectroscopy. The systematic investigations demonstrated that the $\text{Eu}^{3+}:\text{CaF}_2$ fluoride nanocrystals dispersed in sol-gel glass-ceramic materials showed the prolonged luminescence lifetimes of the 5D_0 excited state of Eu^{3+} ions. The significant changes in calculated R/O-ratio values and in luminescence decay profiles clearly indicated the

successful entering of Eu^{3+} ions into CaF_2 nanocrystals during the controlled ceramization process at 350°C . It suggests that sol-gel glass-ceramic materials containing $\text{CaF}_2:\text{Eu}^{3+}$ fluoride nanocrystals are promising candidates for reddish-orange photoluminescence applications.

Author Contributions: N.P., B.S.-S., T.G. and W.A.P. conceived and designed the experiments; N.P., B.S.-S. and T.G. performed the experiments; N.P. and W.A.P. analyzed the data; N.P., B.S.-S., T.G. and W.A.P. contributed reagents/materials/analysis tools; N.P. and W.A.P. wrote the paper.

Funding: This research was funded by National Science Centre (Poland), grant number 2016/23/B/ST8/01965.

Conflicts of Interest: The authors declare no conflicts of interest.

References

1. Beall, G.H.; Pinckney, L.R. Nanophase Glass-Ceramics. *J. Am. Ceram. Soc.* **1999**, *82*, 5–16. [[CrossRef](#)]
2. Ferrari, M.; Righini, G.C. Glass-ceramic materials for guided-wave optics. *Int. J. Appl. Glass Sci.* **2015**, *6*, 240–248. [[CrossRef](#)]
3. Fujita, S.; Tanabe, S. Glass-ceramics and solid-state lighting. *Int. J. Appl. Glass Sci.* **2015**, *6*, 356–363. [[CrossRef](#)]
4. Berneschi, S.; Soria, S.; Righini, G.C.; Alombert-Goget, G.; Chiappini, A.; Chiasera, A.; Jestin, Y.; Ferrari, M.; Guddala, S.; Moser, E.; et al. Rare-earth-activated glass-ceramic waveguides. *Opt. Mater.* **2010**, *32*, 1644–1647. [[CrossRef](#)]
5. Gorni, G.; Velázquez, J.J.; Mosa, J.; Balda, R.; Fernández, J.; Durán, A.; Castro, Y. Transparent glass-ceramics produced by sol-gel: A suitable alternative for photonic materials. *Materials* **2018**, *11*, 212. [[CrossRef](#)]
6. Sharma, R.K.; Mudring, A.-V.; Ghosh, P. Recent trends in binary and ternary rare-earth fluoride nanophosphors: How structural and physical properties influence optical behavior. *J. Lumin.* **2017**, *189*, 44–63. [[CrossRef](#)]
7. Rüssel, C. Nanocrystallization of CaF_2 from $\text{Na}_2\text{O}/\text{K}_2\text{O}/\text{CaO}/\text{CaF}_2/\text{Al}_2\text{O}_3/\text{SiO}_2$ glasses. *Chem. Mater.* **2005**, *17*, 5843–5847. [[CrossRef](#)]
8. Wang, Z.; Cheng, L. Effect of substitution of SiO_2 by CaO/CaF_2 on structure and synthesis of transparent glass-ceramics containing CaF_2 nanocrystals. *J. Mater. Sci.* **2015**, *50*, 4066–4074. [[CrossRef](#)]
9. Chen, D.; Wang, Y.; Yu, Y.; Ma, E.; Hu, Z. Spectroscopic properties of Er^{3+} ions in transparent oxyfluoride glass-ceramics containing CaF_2 nano-crystals. *J. Phys. Condens. Matter* **2005**, *17*, 6545–6557. [[CrossRef](#)]
10. Qiao, X.; Fan, X.; Wang, J.; Wang, M. Luminescence behavior of Er^{3+} ions in glass-ceramics containing CaF_2 nanocrystals. *J. Non-Cryst. Solids* **2005**, *351*, 357–363. [[CrossRef](#)]
11. Hu, Z.; Wang, Y.; Ma, E.; Bao, F.; Yu, Y.; Chen, D. Crystallization and spectroscopic properties investigations of Er^{3+} doped transparent glass ceramics containing CaF_2 . *Mater. Res. Bull.* **2006**, *41*, 217–224. [[CrossRef](#)]
12. Chen, D.; Wang, Y.; Yu, Y.; Ma, E.; Bao, F.; Hu, Z.; Cheng, Y. Luminescence at $1.53\ \mu\text{m}$ for a new Er^{3+} -doped transparent oxyfluoride glass ceramic. *Mater. Res. Bull.* **2006**, *41*, 1112–1117. [[CrossRef](#)]
13. Chen, D.; Wang, Y.; Yu, Y.; Ma, E. Improvement of Er^{3+} emissions in oxyfluoride glass ceramic nano-composite by thermal treatment. *J. Solid State Chem.* **2006**, *179*, 1445–1452. [[CrossRef](#)]
14. Chen, D.; Wang, Y.; Yu, Y.; Ma, E.; Bao, F.; Hu, Z.; Cheng, Y. Influences of Er^{3+} content on structure and upconversion emission of oxyfluoride glass ceramics containing CaF_2 nanocrystals. *Mater. Chem. Phys.* **2006**, *95*, 264–269. [[CrossRef](#)]
15. Kishi, Y.; Tanabe, S. Infrared-to-visible upconversion of rare-earth doped glass ceramics containing CaF_2 crystals. *J. Alloys Compd.* **2006**, *408–412*, 842–844. [[CrossRef](#)]
16. Chen, D.; Wang, Y.; Yu, Y.; Hu, Z. Crystallization and fluorescence properties of Nd^{3+} -doped transparent oxyfluoride glass ceramics. *Mater. Sci. Eng. B* **2005**, *123*, 1–6. [[CrossRef](#)]
17. Chen, D.; Wang, Y.; Yu, Y.; Ma, E.; Liu, F. Fluorescence and Judd-Ofelt analysis of Nd^{3+} ions in oxyfluoride glass ceramics containing CaF_2 nanocrystals. *J. Phys. Chem. Solids* **2007**, *68*, 193–200. [[CrossRef](#)]
18. Babu, P.; Jang, K.H.; Rao, C.S.; Shi, L.; Jayasankar, C.K.; Lavín, V.; Seo, H.J. White light generation in Dy^{3+} -doped oxyfluoride glass and transparent glass-ceramics containing CaF_2 nanocrystals. *Opt. Express* **2011**, *19*, 1836–1841. [[CrossRef](#)]
19. Okada, G.; Ueda, J.; Tanabe, S.; Belev, G.; Wysokinski, T.; Chapman, D.; Tonchev, D.; Kasap, S. Samarium-doped oxyfluoride glass-ceramic as a new fast erasable dosimetric detector material for microbeam radiation cancer therapy applications at the Canadian Synchrotron. *J. Am. Ceram. Soc.* **2014**, *97*, 2147–2153. [[CrossRef](#)]

20. Pawlik, N.; Szpikowska-Sroka, B.; Goryczka, T.; Pisarski, W.A. Photoluminescence investigation of sol-gel glass-ceramic materials containing SrF₂:Eu³⁺ nanocrystals. *J. Alloys Compd.* **2019**, *810*, 151935. [[CrossRef](#)]
21. Innocenzi, P. Infrared spectroscopy of sol-gel derived silica-based films: A spectra-microstructure overview. *J. Non Cryst. Solids* **2003**, *316*, 309–319. [[CrossRef](#)]
22. He, S.; Huang, D.; Bi, H.; Li, Z.; Yang, H.; Cheng, X. Synthesis and characterization of silica aerogels dried under ambient pressure bed on water glass. *J. Non Cryst. Solids* **2015**, *410*, 58–64. [[CrossRef](#)]
23. Sun, X.; Zhang, Y.W.; Du, Y.P.; Yan, Z.G.; Si, R.; You, L.P.; Yan, C.H. From Trifluoroacetate Complex precursors to Monodisperse Rare-Earth Fluoride and Oxyfluoride Nanocrystals with Diverse Shapes through Controlled Fluorination in Solution Phase. *Chem. Eur. J.* **2007**, *13*, 2320–2332. [[CrossRef](#)] [[PubMed](#)]
24. Withers, S.H.; Peale, R.E.; Schulte, A.F.; Braunstein, G.; Beck, K.M.; Hess, W.P.; Reeder, R.J. Broad distribution of crystal-field environments for Nd³⁺ in calcite. *Phys. Chem. Miner.* **2003**, *30*, 440–448. [[CrossRef](#)]
25. Qin, D.; Tang, W. Energy transfer and multicolor emission in single-phase Na₅Ln(WO₄)₄₋₂(MoO₄)₄:Tb³⁺,Eu³⁺ (Ln = La, Y, Gd) phosphors. *RSC Adv.* **2016**, *6*, 45376–45385. [[CrossRef](#)]
26. Zhou, B.E.; E, C.Q.; Bu, Y.Y.; Meng, L.; Yan, X.H.; Wang, X.F. Temperature-controlled downconversion luminescence behavior of Eu³⁺-doped transparent MF₂ (M = Ba, Ca, Sr) glass ceramics. *Luminescence* **2017**, *32*, 195–200. [[CrossRef](#)] [[PubMed](#)]
27. Deng, W.; Cheng, J.-S. New transparent glass-ceramics containing large grain Eu³⁺:CaF₂ nanocrystals. *Mater. Lett.* **2012**, *73*, 112–114. [[CrossRef](#)]
28. Li, Y.; Zhao, L.; Zhang, Y.; Ma, J. Preparation and luminescence properties of Eu³⁺ doped oxyfluoride borosilicate glass ceramics. *J. Rare Earth* **2012**, *31*, 1195–1198. [[CrossRef](#)]
29. Qiao, X.; Luo, Q.; Fan, X.; Wang, M. Local vibration around rare earth ions in alkaline earth fluorosilicate transparent glass and glass ceramics using Eu³⁺ probe. *J. Rare Earth.* **2008**, *26*, 883–888. [[CrossRef](#)]
30. Secu, M.; Secu, C.E.; Ghica, C. Eu³⁺-doped CaF₂ nanocrystals in sol-gel derived glass-ceramics. *Opt. Mater.* **2011**, *33*, 613–617. [[CrossRef](#)]
31. Yanes, A.C.; del-Castillo, J.; Méndez-Ramos, J.; Rodríguez, V.D.; Torres, M.E.; Arbiol, T. Luminescence and structural characterization of transparent nanostructures Eu³⁺-doped LaF₃-SiO₂ glass-ceramics prepared by sol-gel method. *Opt. Mater.* **2007**, *29*, 999–1003. [[CrossRef](#)]
32. Pan, J.; Zhong, K.; Zhang, Z.; Chen, W.; Lin, Y.; Wang, Q.; Li, L.; Yu, Y. Using CaF₂:Eu³⁺ powder as luminescent probe to detect Cr₂O₇²⁻ ions: A new application on the environmental conservation of an old optical material. *Opt. Mater. Express* **2018**, *8*, 2782–2794. [[CrossRef](#)]
33. Binnemans, K. Interpretation of europium (III) spectra. *Coord. Chem. Rev.* **2015**, *295*, 1–45. [[CrossRef](#)]
34. Gökçe, M.; Şentürk, U.; Uslu, D.K.; Burgaz, G.; Şahin, Y.; Gökçe, A.G. Investigation of europium concentration dependence on the luminescent properties of borogermanate glasses. *J. Lumin.* **2017**, *192*, 263–268. [[CrossRef](#)]
35. Sołtys, M.; Janek, J.; Żur, L.; Pisarska, J.; Pisarski, W.A. Compositional-dependent europium-doped lead phosphate glasses and their spectroscopic properties. *Opt. Mater.* **2015**, *40*, 91–96. [[CrossRef](#)]
36. Hehlen, M.P.; Cockroft, N.J.; Gosnell, T.R. Spectroscopic properties of Er³⁺- and Yb³⁺-doped soda-lime silicate and aluminosilicate glasses. *Phys. Rev. B* **1997**, *56*, 9302–9318. [[CrossRef](#)]
37. Van Dijk, J.M.F.; Schuurmans, M.F.H. On the nonradiative and radiative decay rates and a modified exponential energy gap law for 4f-4f transitions in rare-earth ions. *J. Chem. Phys.* **1983**, *78*, 5317–5323. [[CrossRef](#)]
38. Herrmann, A.; Rüssel, C. New Aluminosilicate Glasses as High-Power Laser Materials. *Int. J. Appl. Glass Sci.* **2015**, *6*, 210–219. [[CrossRef](#)]
39. Brown, M.R.; Roots, K.G.; Williams, J.M. Experiments on Er³⁺ in SrF₂. II. Concentration Dependence of Site Symmetry. *J. Chem. Phys.* **1969**, *50*, 891–899. [[CrossRef](#)]
40. Ritter, B.; Haida, P.; Fink, F.; Krahl, T.; Gawlitza, K.; Rurack, K.; Scholz, G.; Kemnitz, E. Novel and easy access to highly luminescent Eu and Tb doped ultra-small CaF₂, SrF₂ and BaF₂ nanoparticles—Structure and luminescence. *Dalton Trans.* **2017**, *46*, 2925–2936. [[CrossRef](#)]

